

See discussions, stats, and author profiles for this publication at: <https://www.researchgate.net/publication/274722003>

# Direct Identification and Analysis of Heavy Metals in Solution (Hg, Cu, Pb, Zn, Ni) using In-Situ Electrochemical X-Ray Fluorescence

ARTICLE in ANALYTICAL CHEMISTRY · APRIL 2015

Impact Factor: 5.64 · DOI: 10.1021/acs.analchem.5b00597 · Source: PubMed

---

CITATION

1

---

READS

61

3 AUTHORS, INCLUDING:



[Mark Edward Newton](#)

The University of Warwick

105 PUBLICATIONS 1,784 CITATIONS

SEE PROFILE



[Julie V Macpherson](#)

The University of Warwick

175 PUBLICATIONS 5,625 CITATIONS

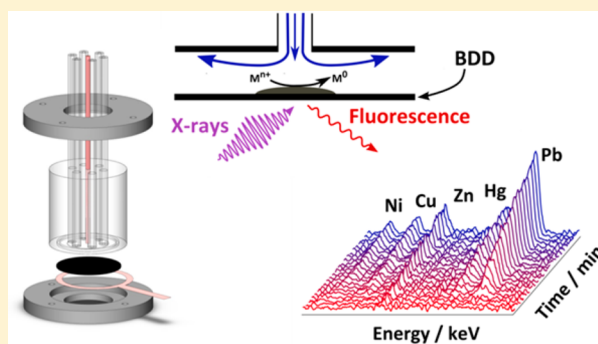
SEE PROFILE

## Direct Identification and Analysis of Heavy Metals in Solution (Hg, Cu, Pb, Zn, Ni) by Use of in Situ Electrochemical X-ray Fluorescence

Glen D. O'Neil,<sup>†</sup> Mark E. Newton,<sup>‡</sup> and Julie V. Macpherson<sup>\*,†</sup><sup>†</sup>Department of Chemistry and <sup>‡</sup>Department of Physics, University of Warwick, Coventry CV4 7AL, United Kingdom

## S Supporting Information

**ABSTRACT:** The development and application of a new methodology, in situ electrochemical X-ray fluorescence (EC-XRF), is described that enables direct identification and quantification of heavy metals in solution. A freestanding film of boron-doped diamond serves as both an X-ray window and the electrode material. The electrode is biased at a suitable driving potential to electroplate metals from solution onto the electrode surface. Simultaneously, X-rays that pass through the back side of the electrode interrogate the time-dependent electrodeposition process by virtue of the XRF signals, which are unique to each metal. In this way it is possible to *unambiguously* identify which metals are in solution and relate the XRF signal intensity to a concentration of metal species in solution. To increase detection sensitivity and reduce detection times, solution is flown over the electrode surface by use of a wall-jet configuration. Initial studies focused on the in situ detection of Pb<sup>2+</sup>, where concentration detection limits of 99 nM were established in this proof-of-concept study (although significantly lower values are anticipated with system refinement). This is more than 3 orders of magnitude lower than that achievable by XRF alone in a flowing solution (0.68 mM). In situ EC-XRF measurements were also carried out on a multimetal solution containing Hg<sup>2+</sup>, Pb<sup>2+</sup>, Cu<sup>2+</sup>, Ni<sup>2+</sup>, Zn<sup>2+</sup>, and Fe<sup>3+</sup> (all at 10  $\mu$ M concentration). Identification of five of these metals was possible in one simple measurement. In contrast, while anodic stripping voltammetry (ASV) also revealed five peaks, peak identification was not straightforward, requiring further experiments and prior knowledge of the metals in solution. Time-dependent EC-XRF nucleation data for the five metals, recorded simultaneously, demonstrated similar deposition rates. Studies are now underway to lower detection limits and provide a quantitative understanding of EC-XRF responses in real, multimetal solutions. Finally, the production of custom-designed portable in situ EC-XRF instrumentation will make heavy metal analysis at the source a very realistic possibility.



Heavy metal contamination caused by increased industrialization is a well-documented, serious problem due to the negative effects these chemical species have on human health and safety and the environment.<sup>1</sup> Heavy metals are not biodegradable and can accumulate in vital organs such as the liver and kidneys, as well as the central nervous system.<sup>2,3</sup> As a result, long-term exposure to even trace levels can be potentially disastrous. This is further exacerbated by considering that humans are at the top of the food chain, and ingesting foodstuffs contaminated with heavy metals will have the same effects as direct exposure. For these reasons, world governments now place strict guidelines on acceptable levels.<sup>4,5</sup>

Many techniques exist for identifying and quantifying trace levels of heavy metals, including inductively coupled plasma mass spectrometry,<sup>6</sup> atomic absorption and emission<sup>7</sup> and colorimetric methods based on host–guest chemistry.<sup>8,9</sup> These methods can be high in cost, require complex sample or substrate preparation, and are often nonportable, which limits their use to the laboratory. Portable, low-cost electrochemical methods, such as anodic stripping voltammetry (ASV)<sup>10,11</sup> and potentiometry using ion-selective electrodes (ISEs)<sup>12,13</sup> have showed promise for trace analysis in situ. However, these

electrochemical techniques often suffer when placed in “real” unknown multimetal solutions, due to the complexities of stripping peak interpretation (for ASV)<sup>14,15</sup> and coextraction (for ISEs),<sup>12,16</sup> making absolute quantification very difficult.

Energy-dispersive (ED) X-ray fluorescence spectroscopy (XRF), which enables chemical identification of individual elements present in a sample, is commonly used for the detection of heavy metals, typically at the parts per million (ppm) level, but is mostly employed with solid samples and powders, due to experimental setup.<sup>17–19</sup> Increased detection sensitivity can be attained through the use of total reflection XRF, which reduces background scatter.<sup>20,21</sup> Direct XRF analysis of liquid (aqueous) samples is possible, but detection limits are severely limited (vide infra).<sup>22</sup> In order to increase detection sensitivity, the solution is often evaporated onto a suitable carrier, leaving the salt for analysis.<sup>23</sup>

Received: February 12, 2015

Accepted: April 9, 2015

Recently, we introduced electrochemical X-ray fluorescence (EC-XRF), as a means to chemically identify trace metals in solution at sub-parts per billion (sub-ppb) levels.<sup>24</sup> Electrochemical deposition was used to preconcentrate heavy metals from solution onto a freestanding polycrystalline boron-doped diamond electrode (BDD), which serves as an excellent EC-XRF substrate due to its wide solvent window, low background currents,<sup>25</sup> and low background fluorescence of carbon and boron. However, the XRF measurements took place *ex situ* with the electrode removed from solution and analyzed on the benchtop.

To address the issue of portability and measurement at the source, we present *in situ* EC-XRF methodology, which enables simultaneous electrodeposition of metals on the electrode surface coupled with XRF analysis, paving the way for *in situ* identification and analysis of heavy metals, using this technology. Here, solution is delivered to the BDD thin ( $\sim 250\ \mu\text{m}$ ) window electrode by use of a wall-jet type electrode configuration, to increase detection sensitivities and decrease analysis times compared to stationary solutions. Preconcentration of the metal takes place on the upper electrode surface, while the high-energy X-rays used to excite the fluorescence pass through from the back face. The secondary “fluorescent” X-rays emitted by the electrodeposited metal pass through the BDD to the detector positioned below, as shown in Figure 1a. The use of thin BDD window electrodes reduces background X-ray scatter from the electrode matrix.

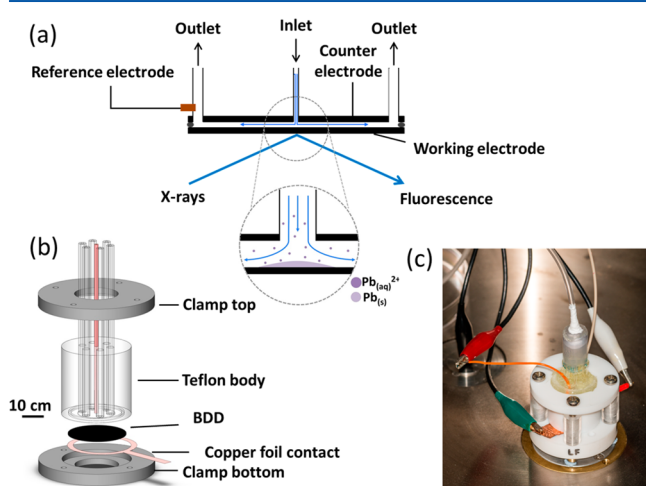


**Figure 1.** Experimental configuration of *in situ* EC-XRF device. (a) Schematic of wall-jet EC-XRF cell and mode of operation; (b) schematic of device assembly; (c) photograph of wall-jet device inside X-ray chamber.

Using *in situ* EC-XRF, we demonstrate that both single ( $\text{Pb}^{2+}$ ) and complex ( $\text{Hg}^{2+}$ ,  $\text{Cu}^{2+}$ ,  $\text{Pb}^{2+}$ ,  $\text{Ni}^{2+}$ ,  $\text{Zn}^{2+}$ ) mixtures of heavy metals can be unambiguously identified in solution at low concentrations, suggesting that field-based measurements in real environments is a future possibility. In this first demonstration, detection sensitivities of  $\sim 10\text{s}$  ppb are reported but further increases are achievable with system refinement. The approach also, interestingly, enables real-time information to be acquired on metal deposition, which is likely to be of interest in understanding electrodeposition characteristics, especially in multiple metal environments.

## EXPERIMENTAL SECTION

**Materials.** Hexaamineruthenium(III) chloride ( $[\text{Ru}(\text{NH}_3)_6]\text{Cl}_3$ , Acros Organics); lead(II) nitrate  $[\text{Pb}(\text{NO}_3)_2]$ ; 99.999%, trace metal basis], copper(II) nitrate  $[\text{Cu}(\text{NO}_3)_2]$ ; 99.999%, trace metal basis], nickel(II) nitrate hexahydrate  $[\text{Ni}(\text{NO}_3)_2 \cdot (\text{H}_2\text{O})_6]$ ; 99.999%, zinc(II) nitrate hexahydrate  $[\text{Zn}(\text{NO}_3)_2 \cdot (\text{H}_2\text{O})_6]$ ; 98%, iron(III) chloride ( $\text{FeCl}_3$ ; 99.99%, trace metal basis), and potassium nitrate ( $\text{KNO}_3$ ), all from Sigma–Aldrich, were used as received. Mercury(II) nitrate monohydrate  $[\text{Hg}(\text{NO}_3)_2 \cdot \text{H}_2\text{O}]$ ;  $>98.5\%$  was from Merck. All solutions were prepared with  $18.2\ \text{M}\Omega \cdot \text{cm}^{-1}$  deionized water (Millipore). Solution pH was measured with a Mettler–Toledo glass-membrane pH electrode. Freestanding, conducting polycrystalline BDD wafers with boron concentrations  $\sim 3 \times 10^{20}\ \text{cm}^{-3}$  and polished to  $250\ \mu\text{m}$  thickness, with a root-mean-square (rms) surface roughness  $<5\ \text{nm}$ , were supplied by Element Six Ltd. (Harwell, U.K.). The wafers were laser-machined into 25 mm diameter (working) and 16 mm diameter (counter) electrodes via laser micromachining methodologies described previously.<sup>26</sup> Prior to use, BDD electrodes were acid-cleaned by boiling in concentrated  $\text{H}_2\text{SO}_4$  (98%), supersaturated with  $\text{KNO}_3$  in order to remove any non-diamond-carbon (NDC) from the laser micromachining process.<sup>27</sup> BDD 1 mm diameter glass-sealed macroelectrodes were prepared as described previously.<sup>26,28</sup>

**In Situ Electrochemical X-ray Fluorescence Apparatus and Operation.** The *in situ* EC-XRF electrochemical cell is based upon a wall-jet configuration, in which an impinging jet of solution flows axially onto the electrode surface and, upon contact, radially across the electrode surface.<sup>29,30</sup> The structural components of the cell, which defined the positions of the inlets, outlets, and working, counter, and reference electrodes, as well as the top and bottom clamp, were machined in-house from Teflon according to the drawing shown in Figure 1b. The design contains a single  $500\ \mu\text{m}$  diameter inlet, which is placed in the center of Teflon block. In order to maintain uniform hydrodynamics within the cell, the single inlet empties into six outlets ( $1.6\ \text{mm}$  i.d.), which are evenly spaced in the cell at positions in line with the circumference of the working electrode. In order to maintain an even pressure drop between the inlet and outlets, all six sections of outlet tubing were epoxied into a custom manifold to form a single waste outlet. All of the tubing was fixed in place with Araldite 5 min epoxy. Fluid flow was controlled by use of an HPLC pump (Gilson Model 305, France) flowing through a manometric module to decrease noise (Gilson model 806, France).

In order to form an electrochemical cell, the Teflon body was placed directly on top of the BDD electrode and assembled with a clamp and M4 screws (Figure 1b). A 2.0 cm diameter O-ring was employed to create a leak-proof seal and determine the diameter of the working electrode. The channel height was fixed to be  $>200\ \mu\text{m}$  (actual height measured by interferometry is  $650 \pm 10\ \mu\text{m}$ ) such that the jet of solution was well-established before impinging onto the electrode surface.<sup>30</sup> Two counter electrode configurations were initially tested. The first consisted of three Pt wire coils ( $250\ \mu\text{m}$ ; Goodfellow) electrically connected in parallel, which were inserted into three of the six outlets. In the second, the counter was laser-machined from  $350\ \mu\text{m}$  thick freestanding conducting BDD in a shape that matched the underside of the Teflon body (including the inlet hole). A 3 mm diameter hexagonal array of  $60\ \mu\text{m}$  diameter holes was positioned around each of the six

outlets, to increase electrode surface area in order to obtain comparable working and counter electrode areas. The counter electrode was then epoxied (Epoxy Resin RX771C/NC, Aradur Hardener HY1300GB, Robnor Resins) onto the upper wall of the Teflon flow channel so the front face was coplanar with the surrounding Teflon, as shown in Figure 1b.

Ohmic contact to the BDD counter was made by graphitizing a small section of the rear of the electrode, using a laser micromachiner and contacting a Cu wire by use of AgDAG (silver conductive paint; RS Components, Corby, U.K.).<sup>31</sup> Ohmic contact to the BDD working electrode was made by sputtering a thin Ti/Au (10 and 300 nm, respectively) contact onto the back side of the BDD surface and subsequently annealing at 400 °C for 5 h. A thin ring of Cu foil (2.5 cm outer diameter and 2.4 cm outer, 100  $\mu$ m thick) with a 1 cm “tongue” (Figure 1b) was cut and placed between the back side of the BDD disk and the Teflon clamp (Figure 1b) and was used to provide an accessible electrical contact. In all experiments, Ag/AgCl wire placed in one of the outlets was used as a pseudoreference electrode.

**Electrochemical Deposition.** All electrochemical experiments were performed with either an Ivium CompactStat (Alvatek Ltd.) or a CHI 730A (Austin, TX) potentiostat controlled by a PC. Prior to deposition the BDD electrode(s) were cleaned with 0.05  $\mu$ m alumina slurry (Micropolish, Buehler, Germany) by use of a microcloth polishing pad or a disposable cotton bud. Background XRF spectra of the BDD electrode, in air, were collected after cleaning to ensure the surface was metal-free. Metal electrodeposition parameters (deposition potential, flow rate, deposition time) were initially optimized to maximize the XRF signal intensity for Pb<sup>2+</sup> electrodeposition in 0.2 M KNO<sub>3</sub> (pH  $\sim$  5.5) (see Supporting Information section 1), which served as the model heavy metal in these proof-of-concept studies.

**X-ray Fluorescence.** In situ EC-XRF was performed on a commercial ED-XRF instrument (NEX CG, Rigaku, Japan). An X-ray tube containing a Pd anode was run at 50 kV with a 1 mA current with a Mo secondary target ( $K\alpha$  = 17.48 keV). The inlet, outlet, and electrical leads were fed into the instrument through the vacuum inlet at the rear of the vacuum chamber (Figure 1c). In this way the X-ray chamber remained fully sealed during in situ EC-XRF measurements to contain stray X-rays. All spectra were collected under ambient conditions. The sampling time varied, depending on the demands of the experiment, and is described in detail alongside the results. The interrogation area of the X-ray source was elliptical, being  $\sim$ 1.2 cm in the widest part and decreasing to  $\sim$ 1.0 cm in the narrowest. The wall-jet electrode was placed over the X-ray optics, so the X-rays entered from the back side of the electrode. The Cu foil connection faced toward the source. All XRF spectra were collected with the device fully assembled within the X-ray chamber in the configuration shown in Figure 1c.

## RESULTS AND DISCUSSION

**Device Characterization.** A wall-jet configuration was employed as a means of increasing mass transport to the electrode during electrodeposition. In the setup considered, solution axially impinges on the electrode and after contact flows radially across the surface.<sup>30,32</sup> As the nozzle diameter is smaller than the electrode diameter, the highest fluid velocities occur near the center of the electrode and steadily decay toward the edges. This electrode configuration allows for well-defined

and variable mass transport rates, which are necessary for reproducible electrochemical depositions during the preconcentration stage of the experiment.

The electrochemical response of the wall-jet electrode has been well-described in the literature,<sup>32,33</sup> where the limiting current is given by<sup>33</sup>

$$i_{\text{lim}} = 1.597nFk_c R^{3/4} \nu^{-5/12} D^{2/3} a^{-1/2} V_f^{3/4} c^* \quad (1)$$

$n$  is the number of electrons transferred,  $F$  is Faraday's constant (96485 C $\cdot$ mol<sup>-1</sup>),  $k_c$  takes a value between 0.86 and 0.90,  $R$  is electrode radius = 1.0 cm,  $\nu$  is kinematic viscosity,  $D$  is diffusion coefficient,  $a$  is diameter of the inlet = 0.05 cm,  $V_f$  is volume flow rate, and  $c^*$  is bulk concentration. Equation 1 assumes laminar flow across the surface of the electrode and that the wall-jet is not impeded by the top of the channel.

The inset to Figure 2a shows chronoamperometric  $i$ - $t$  curves, recorded over 15 s, for the reduction of 0.5 mM Ru(NH<sub>3</sub>)<sub>6</sub><sup>3+</sup> in 0.2 M KNO<sub>3</sub> for  $V_f$  in the range 0–18 mL $\cdot$ min<sup>-1</sup>. The potential was stepped from 0 V vs Ag/AgCl, where no faradaic reaction occurs, to a potential where the current response is mass-transport-limited (–0.5 V vs Ag/AgCl). At all but the slowest  $V_f$ , the current attains a steady state, with the time taken to reach  $i_{\text{lim}}$  decreasing as  $V_f$  increases. A plot of  $i_{\text{lim}}$  ( $n = 3$ ) versus  $V_f^{3/4}$  is shown in Figure 2a, with a linear regression showing excellent agreement ( $R^2 = 0.9999$ ) between  $i_{\text{lim}}$  and  $V_f^{3/4}$  at flow rates above 10 mL $\cdot$ min<sup>-1</sup>. At the lowest  $V_f$ , the current signal starts to deviate from the theoretical response, which is characteristic of diffusion starting to dominate over convection. The gradient of the linear regression line [ $4.27 (\pm 0.03) \times 10^{-5}$  mA $\cdot$ min<sup>3/4</sup> $\cdot$ mL<sup>-3/4</sup>] agrees very well with that calculated ( $4.1 \times 10^{-5}$  mA $\cdot$ min<sup>3/4</sup> $\cdot$ mL<sup>-3/4</sup>) assuming  $k_c = 0.9$ ,  $R = 1.0$  cm,  $\nu = 8.8 \times 10^{-3}$  cm<sup>2</sup> $\cdot$ s<sup>-1</sup>,  $D = 8.8 \times 10^{-6}$  cm<sup>2</sup> $\cdot$ s<sup>-1</sup>,<sup>34</sup>  $a = 0.05$  cm,  $c^* = 0.5 \times 10^{-6}$  mol $\cdot$ cm<sup>-3</sup>, and  $n = 1$ .

The spectral properties of the electrochemical cell were investigated with the cell simply filled with solution (10  $\mu$ M Pb<sup>2+</sup>) and placed over the X-ray window. Figure 2b shows two XRF spectra over the energy range 6–15 keV (vide infra). Black and red lines show the response when Pt and BDD counter electrodes are employed, respectively. In both cases, there is no evidence of a Pb  $L\alpha$  line at 10.56 keV, indicating that a concentration of 10  $\mu$ M Pb<sup>2+</sup> is well below the limit of detection for Pb<sup>2+</sup> in this configuration. Both counter electrode arrangements show small peaks for Fe  $K\alpha$  and Zn  $K\beta/K\alpha$ . The former is due to Fe present in the stainless steel X-ray chamber, while the Zn peak originates from Zn present in the O-ring used in these studies (validated by XRF experiments not detailed here). The cell containing the Pt counter electrode shows three distinct peaks at 9.4, 11.1, and 12.9 keV corresponding to Pt  $L\alpha$ , Pt  $L\beta$ , and Pt  $L\gamma$  lines. Note that the intensity of Pt  $L\alpha$  masks the Zn  $K\beta$  (9.59 keV) response. Use of a BDD counter electrode obviously removes the Pt XRF spectral lines and hence was used for all further studies.

XRF spectra (from 5.5 to 14 keV), were recorded with solution flowing through the cell at  $V_f = 14$  mL $\cdot$ min<sup>-1</sup> (Figure 2c) for different Pb<sup>2+</sup> concentrations (1–50 mM). The response of the Pb  $L\alpha$  peak intensity correlates well with [Pb<sup>2+</sup>] over the concentration range investigated ( $R^2 = 0.996$ ), with a limit of detection (LOD =  $3\sigma$ , where  $\sigma$  is the standard deviation of the noise) of 0.682 mM. This result establishes a benchmark for XRF-only measurements in flowing solutions (for our setup) and is consistent with previous work where XRF has been used previously to measure metal ion concentrations in solution.<sup>22</sup> This result also highlights that



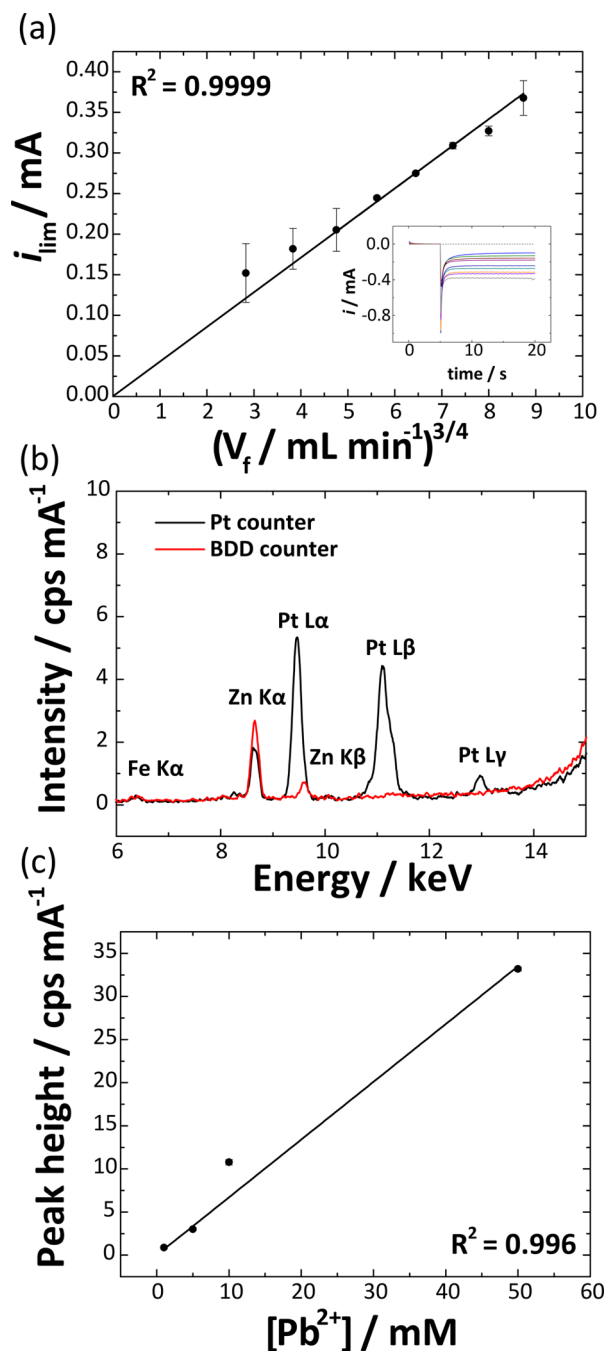


**Figure 2.** Characterization of in situ EC-XRF flow cell. (a)  $i_{\text{lim}}$  versus  $V_f^{3/4}$  (●) for diffusion-limited oxidation of 0.5 mM  $\text{Ru}(\text{NH}_3)_6^{3+}$  in 0.2 M  $\text{KNO}_3$  and comparison with theory (—), eq 1. Inset: Amperometric  $i$ – $t$  curves over the  $V_f$  range 2–18  $\text{mL}\cdot\text{min}^{-1}$ . Error bars represent one standard deviation from three replicate measurements. (b) XRF background spectra collected with either platinum (black line) or BDD (red line) counter electrode positioned within the EC-XRF cell. (c) Quantifying detection limits for XRF-only measurements of  $[\text{Pb}^{2+}]$  in the flow cell. Plot of XRF peak height, measured at 10.56 keV, versus  $[\text{Pb}^{2+}]$  over the range 1–50 mM at  $V_f = 14 \text{ mL}\cdot\text{min}^{-1}$ .

some form of preconcentration is necessary in order to significantly reduce detection sensitivity when making XRF measurements directly in solution.

**In Situ Electrochemical X-ray Fluorescence.** For temporal measurements, it is important to understand the effect of the rate of spectral acquisition on the XRF response.

This was investigated by use of flowing solution ( $V_f = 14 \text{ mL}\cdot\text{min}^{-1}$ ) containing background electrolyte only (0.2 M  $\text{KNO}_3$ ). Figure S2 in Supporting Information, section 2 shows histograms of the peak area recorded over the range 10.1–11 keV, where the Pb  $L\alpha$  peak would reside if  $\text{Pb}^{2+}$  were present in solution. This represents the noise level of the blank signal. Spectra were acquired over 1 h at collection times of 1, 10, 30, and 50 s. As is clear from Figure S2, as collection time decreases, the full width at half-maximum (fwhm) of the “noise” data increases, indicating lower signal-to-noise ratios. As a result, for all the following experiments, an X-ray collection time of 50 s was chosen to maximize detection sensitivity while still maintaining a useful (<1 min) temporal resolution.

To investigate electrochemical preconcentration and showcase the advantages of performing simultaneous electrochemical deposition and temporal analysis in situ by EC-XRF, a solution containing 10  $\mu\text{M}$   $\text{Pb}(\text{NO}_3)_2$  was analyzed. A  $V_f = 14 \text{ mL}\cdot\text{min}^{-1}$  and deposition potential,  $E_{\text{dep}}$ , of  $-1.5 \text{ V}$  vs  $\text{Ag}/\text{AgCl}$  were employed (Supporting Information section 1). Figure 3a displays typical XRF data over the energy window

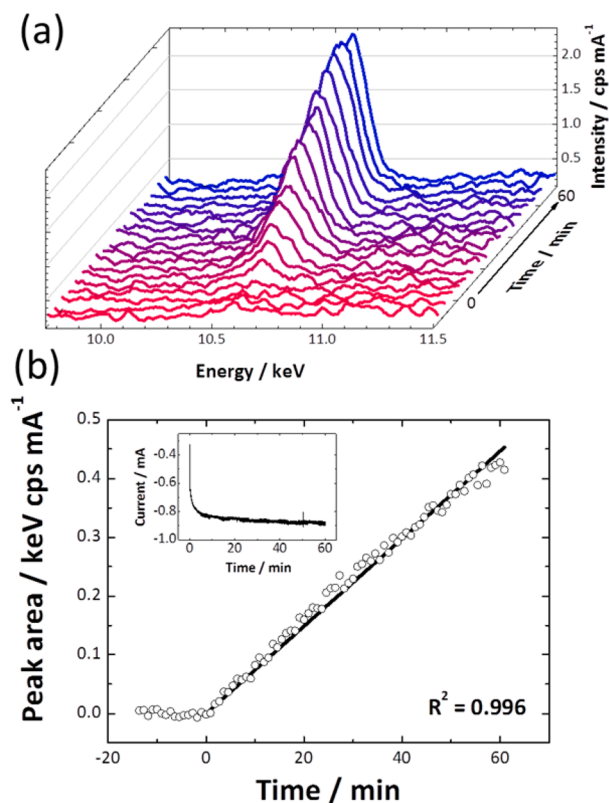


**Figure 3.** Real-time measurement of 10  $\mu\text{M}$   $\text{Pb}^{2+}$  electrodeposition at the BDD electrode by in situ EC-XRF. (a) Plot of Pb XRF intensity over the energy range 9.5–11.5 keV versus time, acquired every 5 min. (b) Plot of XRF Pb  $L\alpha$  peak area from the data in panel a versus time. (Inset) Chronoamperometric  $i$ – $t$  curve for electrochemical deposition carried out in panel a over 60 min.

9.75–11.5 keV (Pb  $L\alpha = 10.56 \text{ keV}$ ) collected at 5 min intervals prior to and during electrochemical deposition ( $t_{\text{dep}} = 60 \text{ min}$ ). The corresponding  $i$ – $t$  curve recorded during electrochemical deposition is shown in the inset to Figure 3b.

The red traces in Figure 3a show three background spectra recorded with no potential bias applied to the electrode. As expected for a 10  $\mu\text{M}$  solution of  $\text{Pb}^{2+}$ , no XRF signature for

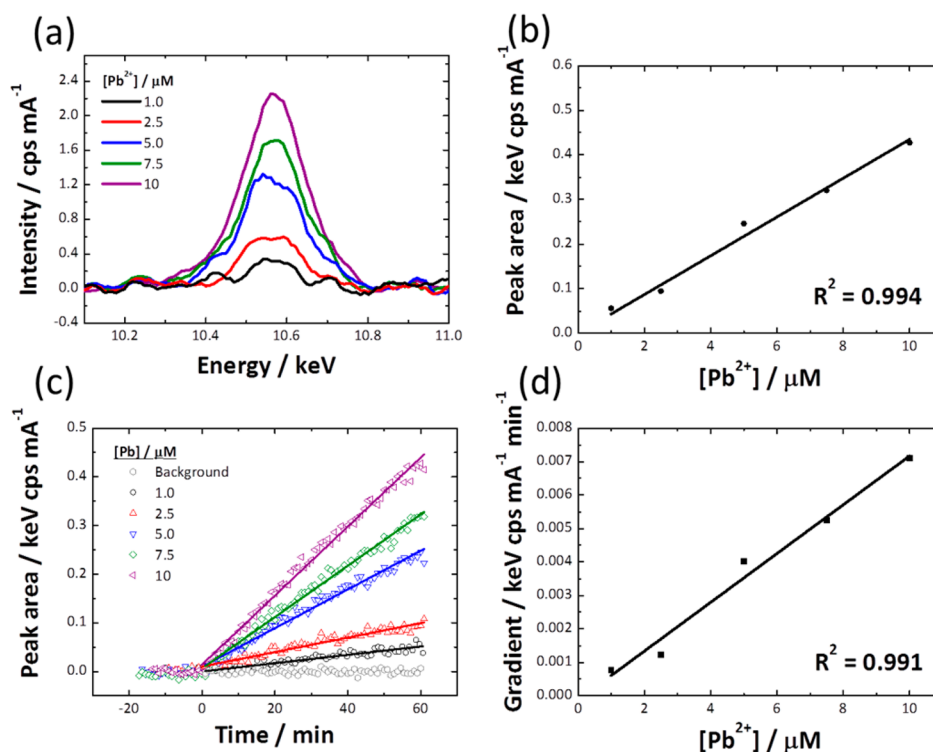


**Figure 4.** (a) XRF intensity versus energy spectra for [Pb<sup>2+</sup>] solutions (in 0.2 M KNO<sub>3</sub>) over concentration range 1–10 μM,  $t_{\text{dep}} = 60$  min, and  $E_{\text{dep}} = -1.5$  V. (b) Plot of peak area versus concentration from the data in panel a. (c) Plot of peak area versus  $t_{\text{dep}}$  for different concentrations investigated. (d) Plot of gradient in panel c vs [Pb<sup>2+</sup>].

Pb<sup>2+</sup> is evident in the region of the Pb *Lα* line. However, under potential bias (purple and blue lines), not only is a signature observed for Pb *Lα* but the Pb *Lα* line grows in intensity with time, due to an increase in the amount of electrodeposited Pb on the electrode surface. The amount of charge passed during electrodeposition was calculated from the  $i$ – $t$  response (shown in the inset to Figure 3b) as 51.4 mC (over 60 min), which corresponds to  $2.7 \times 10^{-7}$  mol of Pb, if it is assumed that the current passed is due only to electroreduction of Pb. This would equate to a maximum volume of  $4.93 \times 10^{-6}$  cm<sup>3</sup> of Pb deposited on the surface (if a density of 11.34 g·cm<sup>-3</sup> is assumed).

To visualize the intensity change in more detail, the acquired spectra were integrated and the resultant peak areas were plotted as a function of  $t$  as shown in Figure 3b. The plot on the time ( $x$ ) axis has been shifted so that electrochemical deposition starts at  $t = 0$  s. Here it can be seen that Pb electrochemical deposition, over this time period and for this starting concentration, shows a linear dependence ( $R^2 = 0.996$ ).

The effect of concentration on the EC-XRF signal was investigated for five concentrations of [Pb<sup>2+</sup>] over the range 1–10 μM, in order to determine the suitability of in situ EC-XRF for quantitative measurements. Data were collected every 50 s, for  $t_{\text{dep}} = 60$  min,  $E_{\text{dep}} = -1.5$  V vs Ag/AgCl, and  $V_f = 14$  mL·min<sup>-1</sup>. Figure 4a shows XRF intensity versus energy spectra, over the range 10.1–11 keV, for the different concentrations investigated at the longest deposition time, that is,  $t_{\text{dep}} = 60$  min, where the signal is largest (as shown in Figure 3a). For each, the Pb *Lα* peak is integrated and plotted versus concentration, as shown in Figure 4b, where a strong correlation between concentration and peak area exists ( $R^2 = 0.994$ ). From this data, the limit of detection, LOD ( $3\sigma$ ), was determined as 99 nM (20.5 ppb), close to the EPA limit for

drinking water (75 nM; 15 ppb).<sup>35</sup> Note that electrochemical preconcentration was recently combined with laser-induced breakdown spectroscopy to detect Zn on Cu electrodes in situ; however, detection limits of only parts per million could be achieved.<sup>36</sup>

From the measurements, it is also possible to produce time-dependent data for each [Pb<sup>2+</sup>] concentration, as shown in Figure 4c. Each data point corresponds to an individual XRF spectrum, collected for 50 s and integrated to calculate the area under the Pb *Lα* line. From Figure 4c it can be clearly seen that the gradient of the peak area versus  $t$  plot, which is itself a measurement of the deposition rate, increases as [Pb<sup>2+</sup>] increases, with a correlation coefficient  $R^2 = 0.991$ . As indicated by Figures 3b and 4c and our previous measurements by ex situ EC-XRF,<sup>24</sup> depositing for longer times, increasing the spectral acquisition time, and further increasing mass transport are some of the ways to increase detection sensitivity by this methodology.

One of the drivers of the development of in situ EC-XRF is as a means to identify, and ultimately quantify, solutions containing multiple metals directly at the source, where the heavy metal composition of the mixture is unknown. In initial preliminary studies aimed at investigating the ability of in situ EC-XRF to detect multiple metals, a solution containing six metals, Fe<sup>3+</sup>, Ni<sup>2+</sup>, Cu<sup>2+</sup>, Zn<sup>2+</sup>, Hg<sup>2+</sup>, and Pb<sup>2+</sup>, at concentrations of 10 μM each, with 0.2 M KNO<sub>3</sub> as supporting electrolyte, was prepared (pH 4.6).

To illustrate the power of in situ EC-XRF, Figure 5a shows the EC-only square wave (SW) stripping voltammetric response (4 mV steps, 10 mV amplitude, 25 Hz) recorded under stirred conditions (magnetic flea), with  $E_{\text{dep}} = -1.5$  V versus Ag/AgCl and  $t_{\text{dep}} = 5$  (red line) and 10 min (black line), using a 1 mm diameter BDD macroelectrode.  $E_{\text{dep}}$  was chosen

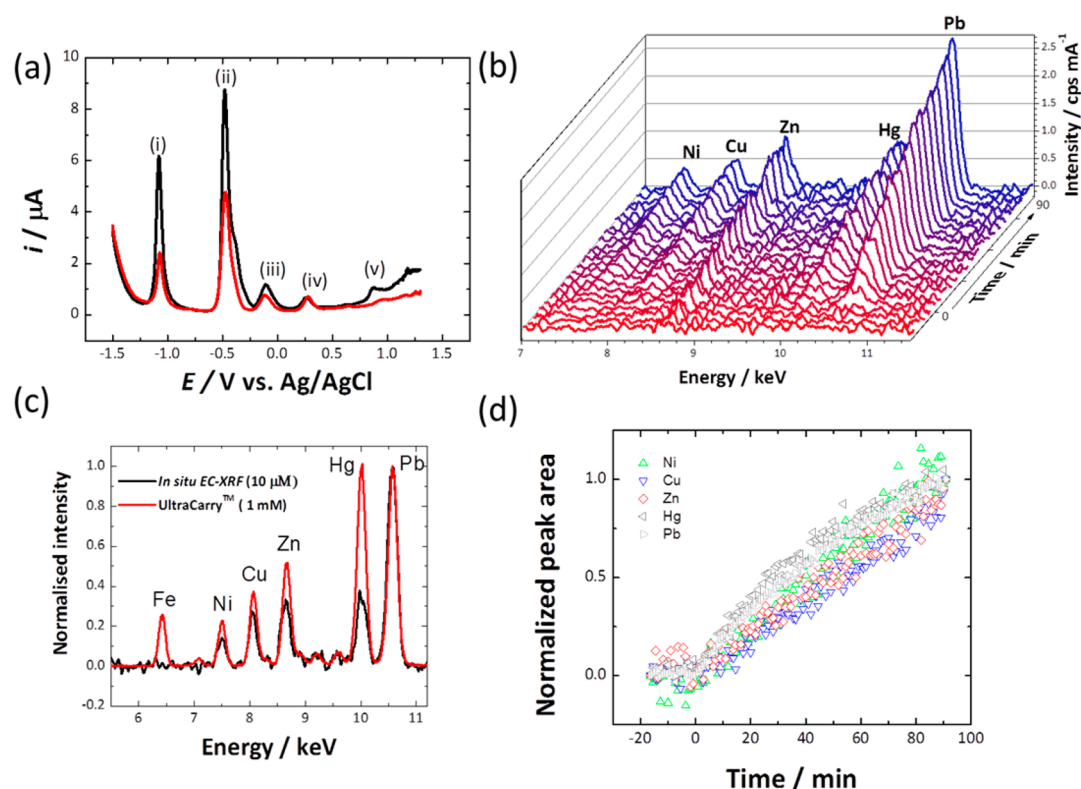


**Figure 5.** (a) Square-wave ASV recorded in a stirred solution containing 10  $\mu\text{M}$  of ions  $\text{Hg}^{2+}$ ,  $\text{Pb}^{2+}$ ,  $\text{Cu}^{2+}$ ,  $\text{Ni}^{2+}$ ,  $\text{Zn}^{2+}$ , and  $\text{Fe}^{3+}$  in 0.2 M  $\text{KNO}_3$  after  $E_{\text{dep}} = -1.5$  V and  $t_{\text{dep}} = 5$  min (red line) and 10 min (black line). (b) EC-XRF recorded in the same solution as in panel a, as a function of time for  $E_{\text{dep}} = 1.5$  V,  $t_{\text{dep}} = 90$  min, and  $V_f = 14$   $\text{mL}\cdot\text{min}^{-1}$ . XRF spectra were recorded every 55 s. XRF enables unambiguous identification of the different elements present on the surface of the electrode. (c) XRF-only spectrum (red line) of the six metals present at 1 mM concentration, evaporatively dried onto an XRF Ultra-Carry substrate, and EC-XRF spectra (black line) taken from panel b at  $t_{\text{dep}} = 90$  min. Note in both cases the data have been normalized with respect to maximum  $\text{Pb}^{2+}$  intensity for respective spectra, to enable a useful comparison. (d) From panel c, plot of peak area versus deposition time for each metal. The data have been normalized with respect to maximum peak area for each metal to enable comparison.

to ensure a sufficiently high driving force for electrodeposition of all six metals. Evident in Figure 5a are five peaks, labeled i–v, occurring at potentials of (i)  $-1.08$ , (ii)  $-0.48$ , (iii)  $-0.10$ , (iv)  $0.26$ , and (v)  $0.87$  V vs Ag/AgCl. Even with prior knowledge of the metals present in solution and consideration of their  $E_0$  values,<sup>37</sup> as listed in Table 1, unambiguous chemical identification of these peaks is challenging. For example, based only on  $E_0$  values and the observed peak positions in Figure 5a, peaks i–v could be tentatively ascribed to (i) Zn, (ii) Ni or Pb, (iii) Fe, (iv) Cu, and (v) Hg. However, as  $E_0$  values do not account for the kinetics of electrodeposition, effects of metal morphology,<sup>15</sup> supporting electrolyte,<sup>38</sup> alloying,<sup>39</sup>

electrocatalysis<sup>40</sup> etc., further experiments are required. These factors also account for the limited application of ASV in complex environmental systems.

Individual SW-ASVs were thus recorded in six individual metal solutions under stirred conditions (10  $\mu\text{M}$  metal salt and 0.2 M  $\text{KNO}_3$ ) with the same electrode and SW-ASV measurement conditions as for Figure 5a with  $t_{\text{dep}} = 5$  min (Supporting Information, section 3). From these data, potentials corresponding to the SW stripping peak currents,  $E_{\text{peak}}$ , were obtained as listed in Table 1. Points of note from Supporting Information, Figure S3 are (i) no evidence of Fe electrodeposition/stripping was observed, (ii) Cu displayed two stripping peaks, (iii) the Ni peak at  $-0.48$  V occurred at a similar potential to Pb but the Pb stripping peak was significantly larger than for Ni, and (iv) there was a second very small Ni stripping peak at  $0.82$  V (observed more readily after  $t_{\text{dep}} = 10$  min). The origin of this second peak is difficult to ascertain; it may be due to oxidation of  $\text{Ni}^{2+}$  [ $\text{Ni}(\text{OH})_2$ ] to  $\text{Ni}^{3+}$  ( $\text{NiOOH}$ ) and is small due to the slightly acidic pH conditions of the solution.<sup>41</sup> From these additional experiments we can now better assign the five SW-ASV peaks to (i) Zn, (ii) Pb and Ni, (iii) Cu, (iv) Hg, and (v) Ni.

In contrast, with in situ EC-XRF, unambiguous identification of the metals present in solution is possible. Figure 5b shows the in situ EC-XRF time-dependent response under experimental conditions  $V_f = 14$   $\text{mL}\cdot\text{min}^{-1}$ ,  $E_{\text{dep}} = -1.5$  V, and  $t_{\text{dep}} = 90$  min; the latter was employed to ensure sufficient deposition resulting in a detectable signal. Note the spectra in Figure 5

**Table 1.**  $E_0$  Values, SW-ASV  $E_{\text{peak}}$  Values, and Energies of the Strongest XRF Emission Peaks<sup>a</sup>

metal	$E_0$ vs NHE, corr against Ag/AgCl <sup>37</sup>	$E_{\text{peak}}$ , V, vs Ag/AgCl	XRF strongest peak intensities, keV
$\text{Hg}^{2+}$	0.60	0.18	9.99 ( $L\alpha$ )
$\text{Cu}^{2+}$	0.14	$-0.17$ and $0.05$	8.05 ( $K\alpha$ )
$\text{Fe}^{3+}$	$-0.24$	$b$	6.41 ( $K\alpha$ )
$\text{Pb}^{2+}$	$-0.33$	$-0.49$	10.56 ( $L\alpha$ )
$\text{Ni}^{2+}$	$-0.53$	$-0.48$ and $0.82$	7.48 ( $K\alpha$ )
$\text{Zn}^{2+}$	$-0.96$	$-1.19$	8.64 ( $K\alpha$ )

<sup>a</sup> $E_0$  values for electrochemical reduction of all six metals, corrected against Ag/AgCl reference electrode, are given. SW-ASV  $E_{\text{peak}}$  values were experimentally measured in individual metal salt solutions. <sup>b</sup>Not available.

have been background-subtracted due to the high Zn background (Figure 2a). With knowledge of the characteristic metal XRF fluorescence lines, also given in Table 1, it is now unequivocally clear which metals have electroplated onto the BDD electrode (Zn, Pb, Ni, Cu, and Hg) and are thus present in the measurement solution. The absence of Fe (no peak was seen at 6.41 keV) correlates with the EC-only data. However, this is not surprising as the literature reports electrodeposition of  $\text{Fe}^{3+}$  is most favored under strongly acidic conditions.<sup>42</sup>

To understand the significance of the peak heights in the EC-XRF spectra, for comparison, an XRF-only spectrum (signal acquisition time = 5 min) of a solution containing the six metals at a concentration of 1 mM each (to ensure a signal would be seen), evaporatively dried (once) onto an Ultracarry XRF substrate (Figure 5c), was recorded (red line). The intensities have been normalized with respect to that for  $\text{Pb}^{2+}$  ( $\text{Pb}^{2+}$  and  $\text{Hg}^{2+}$  gave the highest, very similar peak intensities). The differences in peak intensities for the different metals, all present at the same concentration, reflect the different XRF efficiencies of individual elements.  $\text{Fe}^{3+}$  is clearly present in this spectrum. Also plotted in Figure 5c is the EC-XRF data (black line) from Figure 5b recorded at  $t_{\text{dep}} = 90$  min, also normalized with respect to the highest intensity Pb signal. Qualitatively the EC-XRF signal intensities follow the same trend as for the XRF-only measurements, for all but Hg, boding well for calibration and quantification in mixed-metal solutions. Less Hg than expected was deposited on the BDD electrode, and this could be due to the flow profile of the wall jet washing away some of the electroplated liquid Hg.

When the time-dependent electrodeposition EC-XRF data, plotted as a function of peak area versus time, are displayed, normalized by the maximum peak area for each metal to enable comparison, the gradients appear to overlap (range 0.00959–0.0128  $\text{min}^{-1}$ ;  $0.0114 \pm 0.0013 \text{ min}^{-1}$ ; average  $\pm 1$  standard deviation). The gradients represent the deposition rates of the different metals on the BDD surface and suggest that at the large overpotential employed (for the concentration stated) the deposition rates of all five metals are similar. This also suggests that quantitative analysis in complex mixed-metal solutions by use of EC-XRF is possible.

## CONCLUSIONS

In this paper we introduce in situ EC-XRF as a new methodology to both identify and ultimately quantify heavy metals directly in solution. The EC component employs a freestanding BDD electrode biased at a suitable overpotential to electrodeposit metals from solution onto the electrode. The X-rays pass through the back face of the BDD electrode and are used to directly interrogate the time-dependent XRF profile of the metals as they plate onto the electrode surface. In this way it is both possible to uniquely identify which metals are present in solution (by virtue of their characteristic XRF signature after preconcentration by electrodeposition), monitor metal deposition rates, and ultimately quantify the concentration of metal ions in solution. Solution is flown over the BDD surface in a wall-jet configuration, to enhance mass transport of species to the electrode during deposition.

For direct detection of  $\text{Pb}^{2+}$  in solution, XRF-only measurement results in a LOD of 0.682 mM; however, by switching to EC preconcentration strategies the LOD is reduced to 99 nM (in this present configuration); that is, by over 3 orders of magnitude. LODs could be reduced further, for example, by moving to thinner free-standing BDD electrodes, increasing

mass transport, increasing preconcentration and XRF signal collection times, etc.

Proof-of-concept multimetal detection was demonstrated by using EC-XRF to detect the presence of six metals,  $\text{Hg}^{2+}$ ,  $\text{Pb}^{2+}$ ,  $\text{Cu}^{2+}$ ,  $\text{Ni}^{2+}$ ,  $\text{Zn}^{2+}$ , and  $\text{Fe}^{3+}$  (all at 10  $\mu\text{M}$  concentration in 0.2 M  $\text{KNO}_3$ ) in one solution. Measurements were compared to SW-ASV analysis in the same solution. EC-XRF was able to unequivocally identify five metals in one single measurement. In contrast, ASV required significant further experiments to enable identification of the five peaks evident in the SW-ASV trace. Both studies demonstrated that  $\text{Fe}^{3+}$  did not directly reduce to Fe under the experimental pH conditions employed. Note, we have shown previously that simple electrochemical strategies can be employed to optimize the pH of the measurement environment in situ in order to facilitate the electrochemical measurement of interest.<sup>43,44</sup> Similar strategies could be adopted here, when required.

The relative intensity of the EC-XRF signals correlated with those recorded by XRF only (evaporated samples) for all metals but Hg, suggesting less Hg than expected had plated onto the electrode surface. This is most likely due to some of the liquid metal being washed from the surface during deposition. In situ EC-XRF also enabled the deposition rate of all five metals electroplating on the electrode surface to be monitored. Under the experimental conditions employed, all five showed similar rates, boding well for quantitative analysis. Experiments are now underway to lower detection limits and provide a quantitative understanding of EC-XRF detection in real, multimetal solutions. These are with a view to producing custom-designed portable EC-XRF instrumentation to make sub-pbb heavy metal identification and analysis at the source a realistic possibility.

## ASSOCIATED CONTENT

### Supporting Information

Additional text and three figures describing (1) optimization of electrode deposition parameters for  $\text{Pb}^{2+}$ , (2) effect of rate of spectral acquisition on XRF response, and (3) interpretation of SW-ASV response of an aqueous solution containing six different dissolved metals. This material is available free of charge via the Internet at <http://pubs.acs.org>.

## AUTHOR INFORMATION

### Corresponding Author

\*E-mail [j.macpherson@warwick.ac.uk](mailto:j.macpherson@warwick.ac.uk).

### Notes

The authors declare no competing financial interest.

## ACKNOWLEDGMENTS

We thank Element Six for funding of GDO and for providing the freestanding BDD electrodes used throughout, Dr. Jonathan Newland for the photograph in Figure 1c and for laser-machining the BDD counter electrode, Ronald Wesson and Marcus Grant for assistance in fabricating the devices used herein, and Lingcong Meng for collecting the SW-ASV data.

## REFERENCES

- (1) Jarup, L. *Br. Med. Bull.* **2003**, *68*, 167–182.
- (2) Vallee, B. L.; Ulmer, D. D. *Annu. Rev. Biochem.* **1972**, *41*, 91–128.
- (3) Hamilton, J. W.; Kaltreider, R. C.; Bajenova, O. V.; Ihnat, M. A.; McCaffrey, J.; Turpie, B. W.; Rowell, E. E.; Oh, J.; Nemeth, M. J.; Pesce, C. A.; Lariviere, J. P. *Environ. Health Perspect.* **1998**, *106*, 1005–1015.



- (4) U.S. Environmental Protection Agency. *Risk Assessment, Management and Communication of Drinking Water Contamination*; US EPA 625/4-89/024; EPA: Washington, DC, 1989.
- (5) Off. J. Eur. Union L **2006**, 364, 5–24.
- (6) Aragay, G.; Pons, J.; Merkoçi, A. *Chem. Rev.* **2011**, 111, 3433–3458.
- (7) Bersier, P. M.; Howell, J.; Bruntlett, C. *Analyst* **1994**, 1, 219–232.
- (8) Ariza-Avidad, M.; Salinas-Castillo, A.; Cuéllar, M. P.; Agudo-Acemel, M.; Pegalajar, M. C.; Capitán-Vallvey, L. F. *Anal. Chem.* **2014**, 86, 8634–8641.
- (9) Liu, L.; Lin, H. *Anal. Chem.* **2014**, 86, 8829–8834.
- (10) Herdan, J.; Feeney, R.; Kounaves, S. P.; Storment, C. W.; Kovacs, G. T. A.; Darling, R. B. *Environ. Sci. Technol.* **1998**, 32, 131–136.
- (11) Feeney, R.; Kounaves, S. P. *Anal. Chem.* **2000**, 72, 2222–2228.
- (12) Chumbimuni-Torres, K. Y.; Rubinova, N.; Radu, A.; Kubota, L. T.; Bakker, E. *Anal. Chem.* **2006**, 78, 1318–1322.
- (13) De Marco, R.; Clarke, G.; Pejčić, B. *Electroanalysis* **2007**, 19, 1987–2001.
- (14) Jones, S. E. W.; Chevallier, G.; Paddon, C. A.; Compton, R. G. *Anal. Chem.* **2007**, 79, 4110–4119.
- (15) Hutton, L. A.; Newton, M. E.; Unwin, P. R.; Macpherson, J. V. *Anal. Chem.* **2011**, 83, 735–745.
- (16) Bakker, E.; Bühlmann, P.; Pretsch, E. *Chem. Rev.* **1997**, 97, 3083–3132.
- (17) Bernick, M. B.; Kalnicky, D. J.; Prince, G.; Singhvi, R. J. *Hazard. Mater.* **1995**, 43, 101–110.
- (18) Melquiades, F. L.; Appoloni, C. R. *J. Radioanal. Nucl. Chem.* **2004**, 262, 533–541.
- (19) Jang, M. *Environ. Geochem. Health* **2010**, 32, 207–216.
- (20) Prange, A. *Spectrochim. Acta, Part B* **1989**, 44, 437–452.
- (21) Barreiros, M. A.; Carvalho, M. L.; Costa, M. M.; Marques, M. I.; Ramos, M. T. *X-ray Spectrom.* **1997**, 26, 165–168.
- (22) Peng, S.; Liu, Z.; Sun, T.; Ma, Y.; Ding, X. *Anal. Chem.* **2014**, 86, 362–366.
- (23) Melquiades, F. L.; Parreira, P. S.; Appoloni, C. R.; Silva, W. D.; Lopes, F. *Appl. Radiat. Isot.* **2011**, 69, 327–333.
- (24) Hutton, L. A.; O’Neil, G. D.; Read, T. L.; Ayres, Z. J.; Newton, M. E.; Macpherson, J. V. *Anal. Chem.* **2014**, 86, 4566–4572.
- (25) Macpherson, J. V. *Phys. Chem. Chem. Phys.* **2015**, 17, 2935–2949.
- (26) Hutton, L. A.; Iacobini, J. G.; Bitziou, E.; Channon, R. B.; Newton, M. E.; Macpherson, J. V. *Anal. Chem.* **2013**, 85, 7230–7240.
- (27) Prado, C.; Wilkins, S. J.; Grundler, P.; Marken, F.; Compton, R. G. *Electroanalysis* **2003**, 15, 1011–1016.
- (28) Hutton, L.; Newton, M. E.; Unwin, P. R.; Macpherson, J. V. *Anal. Chem.* **2009**, 81, 1023–1032.
- (29) Soucaze-Guillous, B.; Kutner, W. *Electroanalysis* **1997**, 9, 32–39.
- (30) Bitziou, E.; Rudd, N. C.; Edwards, M. A.; Unwin, P. R. *Anal. Chem.* **2006**, 78, 1435–1443.
- (31) Joseph, M. B.; Bitziou, E.; Read, T. L.; Meng, L.; Palmer, N. L.; Mollart, T. P.; Newton, M. E.; Macpherson, J. V. *Anal. Chem.* **2014**, 86, 5238–5244.
- (32) Chin, T.; Tsang, H. J. *Electrochem. Soc.* **1978**, 125, 1461–1470.
- (33) Brett, C. M. A.; Oliveira Brett, A. M. C. F.; Fisher, A. C.; Compton, R. G. *J. Electroanal. Chem.* **1992**, 334, 57–64.
- (34) Macpherson, J. V.; O’Hare, D.; Unwin, P. R.; Winlove, C. P. *Biophys. J.* **1997**, 73, 2771–2781.
- (35) U.S. Environmental Protection Agency. National Primary Drinking Water Regulations. <http://water.epa.gov/drink/contaminants>.
- (36) Matsumoto, A.; Tamura, A.; Koda, R.; Fukami, K.; Ogata, Y. H.; Nishi, N.; Thornton, B.; Sakka, T. *Anal. Chem.* **2015**, 87, 1655–1661.
- (37) Bard, A. J.; Faulkner, L. R. *Electrochemical Methods: Fundamentals and Applications*, 2nd ed.; Wiley: New York, 2001.
- (38) Saciloto, T. R.; Cervini, P.; Cavaleiro, E. T. G. *Electroanalysis* **2014**, 26, 2664–2676.
- (39) Babyak, C.; Smart, R. B. *Electroanalysis* **2004**, 16, 175–182.
- (40) Prado, C.; Wilkins, S. J.; Marken, F.; Compton, R. G. *Electroanalysis* **2002**, 14, 262–272.
- (41) Bossu, F. P.; Margerum, D. W. *Inorg. Chem.* **1977**, 16, 1210–1214.
- (42) Izaki, M. In *Modern Electroplating*; Schlesinger, M., Paunovic, M., Eds.; John Wiley & Sons, Inc.: Hoboken, NJ, 2010; pp 309–326.
- (43) Read, T. L.; Bitziou, E.; Joseph, M. B.; Macpherson, J. V. *Anal. Chem.* **2014**, 86, 367–371.
- (44) Bitziou, E.; Joseph, M. B.; Read, T. L.; Palmer, N.; Mollart, T.; Newton, M. E.; Macpherson, J. V. *Anal. Chem.* **2014**, 86, 10834–10840.